Non-Intrusive Instrument for Thermal Protection System to Measure Recession and Swelling

Gilles Bailet[1]
EM2C, CNRS, CentraleSupelec, Universite Paris Saclay, Gif-sur-Yvette, 91190, France

Amandine Denis[2]
von Karman Institute for Fluid Dynamics, Rhode-Saint-Genèse, 1640, Belgium

Alexis Bourgoing[3]
ArianeGroup, Les Mureaux, 78133, France

Christophe O. Laux[4]
EM2C, CNRS, CentraleSupelec, Universite Paris Saclay, Gif-sur-Yvette, 91190, France

and
Thierry E. Magin[5]
von Karman Institute for Fluid Dynamics, Rhode-Saint-Genèse, 1640, Belgium

Quantifying the thermal response of a heat shield is a key step in the design of a spacecraft to ensure its survivability during atmospheric entry. Recession and swelling of the thermal protection material have a drastic effect on both the heat transfer within the vehicle and aerothermodynamic transients. Post flight analysis of reentry can be achieved after recovery on Earth, but it is more difficult for entries on other bodies of the solar system. A dedicated instrumentation is necessary to understand the evolution of the thermal protection material thickness during flight. This paper investigates the current limitations of the available measurement techniques. A low-mass passive solution is proposed to measure with high accuracy the phenomena of recession, also valid for materials only subject to sublimation such as polytetrafluoroethylene, and swelling. The QARMAN CubeSat mission provides a flight opportunity to develop a dedicated payload to quantify the recession and swelling of an

[1] Current affiliation: Research associate. Division of System, Power and Energy. James Watt School of Engineering; gilles.bailet@glasgow.ac.uk
[2] Research Engineer, Aeronautics and Aerospace Department; denis@vki.ac.be.
[3] Research Engineer, Aerodynamics and Atmospheric Re-entry Section; alexis.bourgoing@ariane.group.
[4] Professor, Laboratoire EM2C, CNRS UPR288 ; christophe.laux@centralesupelec.fr.
[5] Professor, Aeronautics and Aerospace Department; magin@vki.ac.be.

ablative heat shield made of Cork P50 from Amorim™. In addition, this payload allows us to study the radiation of a reentry plasma in the presence of ablation products through the same optical path. The performance of the measurement technique and the integration of the instrument are discussed for the QARMAN platform, demonstrating its applicability to a space mission.

Nomenclature

A = area of each optical interface, m^2

c = canal radius, m

D = distance to the interface, m

$d\Phi$ = contribution of each light ray, W

I = light intensity, $W.m^{-2}$

l = canal length, m

R = radius of the clear aperture, m

t = time, s

X = X component of center coordinates, m

Y = Y component of center coordinates, m

Z = Z component of center coordinates, m

Θ = half angle of view, rad

θ = elevation of emitted ray, rad

φ = azimuth of emitted ray, rad

Ω = ratio of reference and total intensity

Subscripts

ds = elementary surface

i = value for the i^{th} interface

ref = reference value

ToF = time-of-flight

tot = total integrated value

I.Introduction

Ranging from 10 to 50% of the total mass of a reentry/entry vehicle [1], the Thermal Protection System (TPS) is a critical part of the platform. Current design methods for spacecraft consider the heat shield as one-point failure subsystem, thus adding extra margins to the nominal design. In order to reduce uncertainties on the heat shield performance, measurements of the TPS thickness evolution are necessary.

The shape changes of a heat shield can be measured in ground testing facilities or flight. Traditionally, ground testing facilities use high-speed cameras looking cross flow to track the surface evolution of the material sample. This technique allows us to deduce recession and swelling (RS) of the TPS. In general, ground testing methodologies prevent the full duplication of all entry phenomena occurring at the same time in flight. For instance, the review presented in [2] shows that inductive coupled plasma torches only duplicate stagnation point conditions using a subsonic plasma jet, arc jet tunnels can be used to reach a wider range of testing conditions but the electrode erosion can be detrimental to study gas-surface-interactions, while shock tubes allow for the study of radiation but have short testing duration and are limited to small test articles. Thus, none of the ground testing facilities can be used to study both the radiation and gas-surface-interaction phenomena for full-scale models and transient conditions. When it comes to flight instruments, the use of thermocouples (TCs) has been investigated alternatively in most recent missions [3] to determine the position of the recession front based on their end-of-life. This methodology is however not fully reliable and cannot be extended to measure the swelling of a sample, as it only tracks a specific isotherm corresponding to the maximal temperature that can be measured reliably by a TC within the TPS (type K, N: 1260^{o}C, type R, S: 1450^{o}C [4]). This is clearly insufficient because, as shown in [5], the surface temperature of the TPS during the mission or testing on ground reaches temperatures greater than 2000^{o}C, thus beyond the current capabilities of the different types of TCs. Other methods have been proposed but they can locally change the recession behavior [[6] [7] [8] [9]] or are not compatible with all TPS materials [10]. Despite a high scientific interest, instrumentation capabilities remain limited as they are intrusive, restricted to some classes of materials, or do not allow for measurements for the full duration of the mission.

In this paper, a novel instrument is developed to measure the RS phenomena with a simple and efficient design. A low-mass passive solution is proposed to measure with accuracy the phenomena of recession, also valid for materials only subject to sublimation such as polytetrafluoroethylene, and swelling. Validation tests demonstrated that the optical access of the measurement technique presented in this paper does not influence the RS process, thus, the technique can be considered as non-intrusive for the thermal response of the TPS. Moreover, the payload is able to measure the RS of most TPS materials but additional tests are necessary to find its limits. The QARMAN CubeSat mission provides a flight opportunity to develop a dedicated payload to quantify the recession and swelling of an ablative heat shield made of Cork P50 from Amorim™. The technique developed is applied to this thermal protection material for the QARMAN reentry conditions. In addition, this payload allows us to study the radiation of a reentry plasma in the presence of ablations products through the same optical path.

The paper is organized as follows. The state-of-the-art literature on recession and swelling measurement techniques is reviewed in section II, including some analysis. In section III, the RS instrument concept is introduced, while its technical implementation is discussed in section IV. The performance of the measurement technique is assessed in section V by means of experimental results obtained in the VKI Plasmatron facility. In section VI, the instrument is optimized for its integration and operation on the reentry platform QARMAN, demonstrating its applicability to a space mission.

II. Review of Recession and Swelling Measurement Techniques

The RS phenomena in atmospheric entry flows show their most drastic effect through the shape change of a TPS. They have an impact on the in-depth heat transfer processes and in turn on the aerodynamic coefficients. Several methods exist to perform measurements of the recession of TPS materials. This section reviews the existing instrumentation, together with its advantages, operating range, accuracy, and limitations.

A. ARAD/HEAT Sensor

Developed by NASA [[6] [7]], this recession sensor, shown schematically in Fig. 1, comprises a central core of TPS material surrounded by two wires helicoidally wrapped around it. Recession shortens the length of each wire. As a result, the measured voltage difference between the two wires decreases as the recession front progresses.

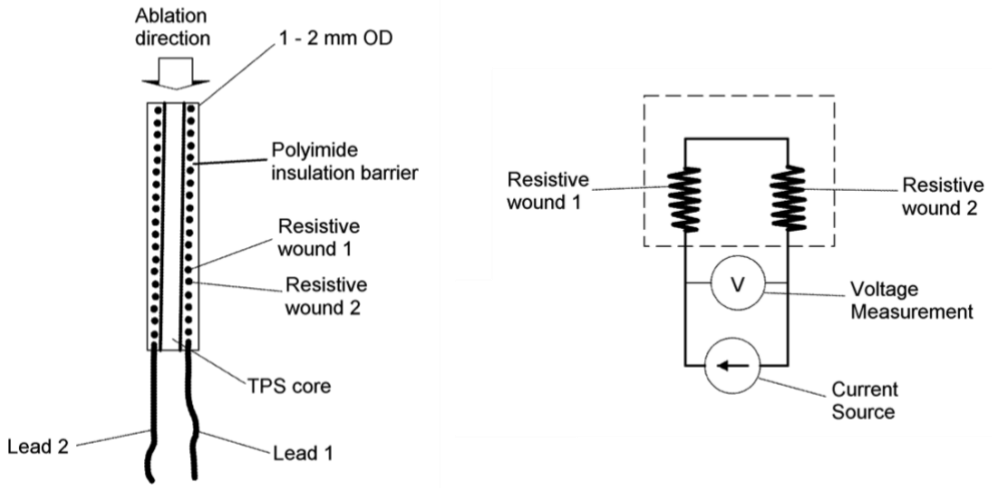

Fig. 1 ARAD/HEAT sensor schematic after [6] (left: cross section; right: electrical circuit).

The accuracy of the technique is determined by the spacing between the spires of the helicoidal wires and is typically ±2mm. It is possible to increase the resolution of the instrument by reducing the diameter of the wires, but this leads to an increase of the noise, which perturbs the measurement. In addition, this measurement technique is highly intrusive and the probe tends to recess at a different speed than the bare TPS, thus adding to the uncertainties. Furthermore, this measurement technique cannot measure neither sublimation nor swelling.

B. MIRRAS probe

The US company Orbitec has developed the MIRRAS probe [8], as a two-dimensional variant of the ARAD probe. The recession measurement is also directly proportional to the voltage between the two leads of the probe. This technique can be used to measure recession of TPS but has never been used for reentry applications. It is optimized for materials with high humidity levels.

C. Fiber-optical sensor

Researchers from the Ukrainian National Academy of Science have developed an optical technique to predict the recession of a TPS [9]. A schematic of the setup is shown in Fig. 2. The concept of the instrument is to integrate optical fibers inside the ablative TPS at different depths within the material. As shown during preliminary tests, when the recession front reaches the location of each optical fiber, a brief impulse of light is detected before the fiber burns. As seen in [11], photodetectors are highly sensitive to temperature changes. Thermo-stabilization was thus carried out

with a cavity surrounding the photodetectors filled with lithium nitrate trihydrate $LiNO_3$-$3H_2O$, a phase change material able to stabilize the temperature of the detectors around 30°C (specific melting heat r = 290 kJ/kg).

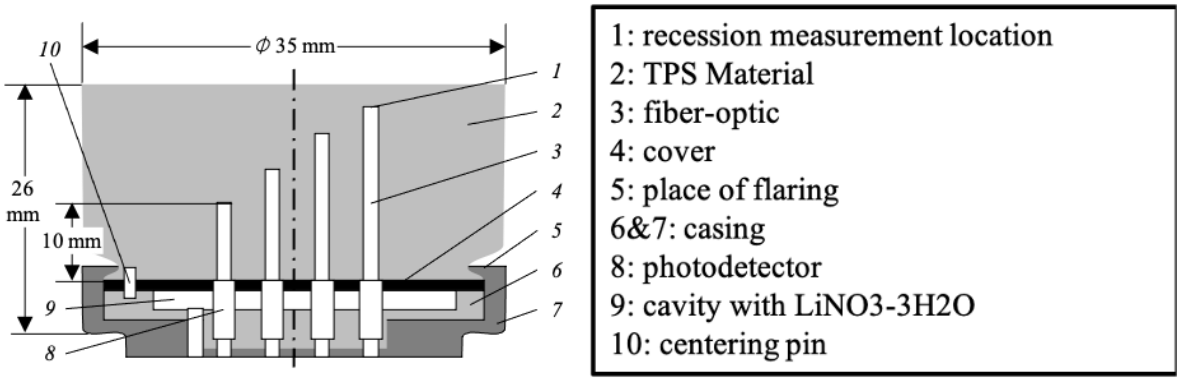

Fig. 2 Structural arrangement of the Fiber-Optic Sensor [9].

This technique has several drawbacks including the limited number of measurement positions and the difference between the melting rate of the optical fibers and certain TPS materials. Moreover, this sensor is not able to measure swelling.

D. Thermocouple-based methods

Numerous flight instrumentation packages include thermocouples [5]. For instance, putting a strong emphasis on reentry vehicle instrumentation, NASA has developed the MEDLI and MEDLI2 payload suites (see Fig. 3) for entry missions [3]. These packages include a HEAT sensor and a suite of four thermocouples (only for MEDLI [12]) located at different depths along the same measurement line perpendicular to the TPS surface.

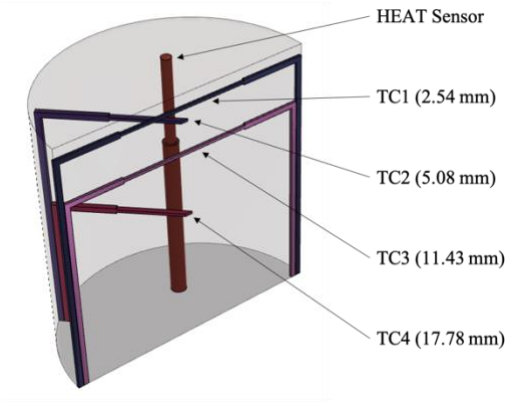

Fig. 3 Cross-view of the MEDLI sensor plug [3] (HEAT: evolution of the ARAD sensor; TC: Thermocouples type K).

These temperature measurements permit to reconstruct the thermal response of the TPS during entry. Some downscaling strategies for low-cost instrumentation packages have been proposed to assess the recession of the TPS without the ARAD/HEAT sensor that is ITAR restricted. To understand the concept of this measurement technique, it is important to delve into the analysis of an example of thermocouple measurements. The measurements shown in Fig. 4 correspond to a Mars entry case at the stagnation point of the Mars Science Laboratory (MSL) (MISP I, [3]).

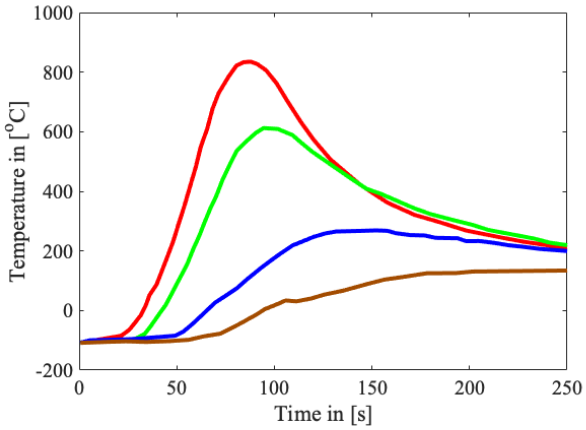

Fig. 4 Temperature profile evolution for MSL mission from [3] at different depths from the surface (red: 2.54 mm; green: 5.08 mm; blue: 11.43 mm; brown: 17.78 mm).

As seen in Fig. 4, the in-depth temperature of the TPS gradually increases, reaches a maximum value, and then decreases. The increase is due to high heat flux impinging on the vehicle (>100 kW/m2). The decrease of temperature is directly linked to the cooled air flow convection appearing at lower altitude, when the vehicle speed decreases below Mach 8, and surface radiation cooling. The MEDLI team intended to detect recession by positioning a thermocouple close to the surface of the TPS. The time corresponding to the end-of-life signal of the device should have indicated the moment at which the recession front had reached the TC location. However, no thermocouple end-of-life signal was received during the MSL entry, indicating that the TC never reached its melting temperature. Table 1 summarizes the different types of TCs and their measurement ranges. Thermocouples are used to measure in-depth temperature profiles. They are composed of two different conductors linked by an electrical junction placed at the location of the measurement. By measuring the voltage difference between the two wires (of the order of mV), the temperature of the junction can be deduced (see for example [13]). Different pairs of conductors have different measurement ranges and noise levels.

Table 1 Types of commercially available thermocouples

TC Type	Metal Pairs	Lower-End of the Temperature Range in [°C]	Upper-End of the Temperature Range in [°C]
K	Chromel/Alumel	-200	1250
C	Tungsten/Rhenium	0	2329
E	Chromel/Constantan	0	900
R	Platinum/Rhodium	0	1450
S	Platinum/Rhodium	0	1450
B	Platinum/Rhodium	0	1700
N	Nicrosil/Nisil	0	1300

As presented in the table, the maximum temperature that can be measured by means of TCs is limited to about 2329°C for type C, whereas TPS surfaces can reach 2000-3000°C. In practice, concerning recession, they only allow us to measure the displacement of an isotherm by tracking the end-of-life of each of the TCs within the payload suite.

E. Ultrasonic sensor-based method

An ultrasonic transducer attached to the backside of a heatshield can be used to measure the ablation and temperature distribution within a TPS material [10]. Using sound waves, such device is able to detect fast thermal response features on the order of 100 microseconds (without thermal lag). This apparatus uses the backscatter from a material's micro- structure to detect interfaces (pyrolysis layer and char layer) as well as temperature distribution using an advance algorithm based on Time-of-Flight time between the ultrasound emission and the echo reception. Fig. 5 demonstrates the detection capabilities of the method for different scenarios (layered sample, sample with a cavity and sample with a step as interface).

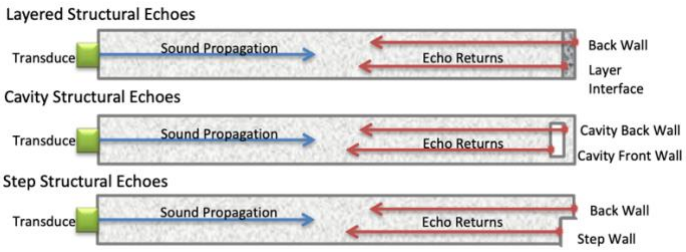

Fig. 5 Ultrasonic TPS recession sensor application to different slab geometries (from [10])

Those scenarios are ideal cases of features found in TPS. The "Layered Structural Echoes" is the ideal case of an ablative TPS with a virgin layer and a char layer. The "Cavity Structural Echoes" represents inclusions or cracks

within the TPS. Finally, the "Step Structural Echoes" represents a simplified case for irregular TPS surface. From this figure, we can see that the distance of the features from the transceiver will give a different ToF for each reflexion hence allowing us, at least theoretically, to distinguish all features on the line-of-sight of the instrument. In practice, results in [14] have studied the limit of the technique, which cannot be used in materials where backscattering is not significant, by introducing embedded reflectors making the sensor highly intrusive for those specific materials. Moreover, Lloyd *et al.* [10] recommend using the technique for high density TPS materials and frequencies in the order of few MHz.

Unfortunately, several heatshield materials used in space missions are characterized by a low density and low backscattering. The reentry vehicle QARMAN, presented in this paper, is equipped with such heatshield (Cork P50 from Amorim^{TM}). Lingblum [15] shows that ultrasounds penetrate extremely poorly in natural cork and cork filled epoxy (similar to Cork P50), following experiments on the TPS of the solid rocket boosters of the space shuttle. Moreover, experiments in [16] indicate that only a combination of terahertz frequencies and natural defects in the cork (cracks, voids as well as variations in the cork cell structure) allow us to obtain back scattering to inspect natural cork samples, hence deviating from the mm-wave strategy used in [10].

The ultrasonic based method is a non-intrusive method to measure RS for a certain class of TPS (high density) but lacks versatility to be used with any type of material. Embedded reflectors as exposed in [13] are suggested to extend the compatibility of the method to low backscattering materials at the disadvantage of becoming highly intrusive.

F. High-speed camera-based measurement technique

This visualization technique is present in modern TPS testing facilities (see for instance [17]) but is unfortunately not applicable to in-flight measurements. It consists in placing a high-speed camera with a line-of-sight perpendicular to the recession direction of interest. The device acquires pictures from which the sample geometry can be extracted over time, hence, measuring the recession and swelling. Fig. 6 presents an example of sample under test and the end result of the technique.

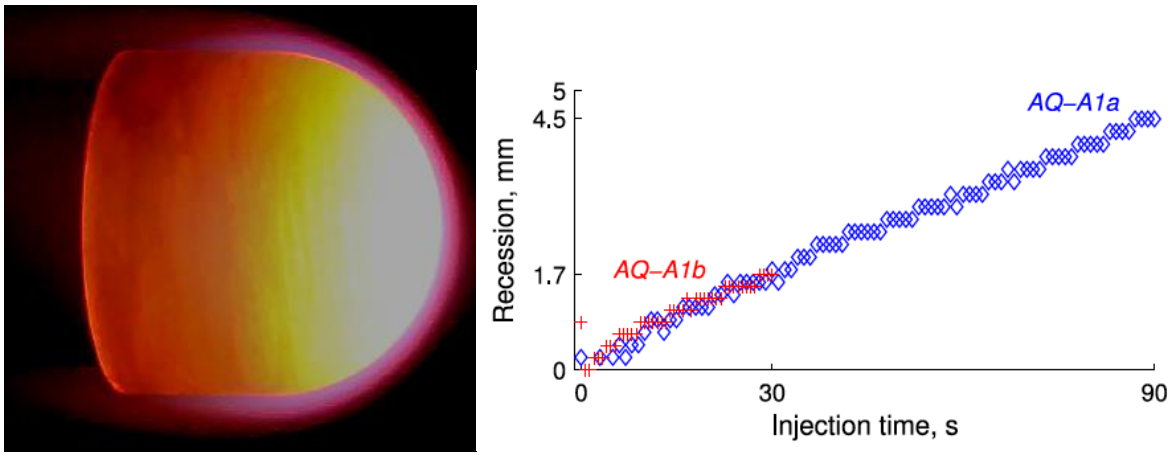

Fig. 6 Example of a high-speed camera-based measurement technique from [18] (left: sample during test; right: surface recession).

As can be seen from Fig. 6, the technique is effective at detecting the surface position of the sample. With careful calibration and alignment, TPS shape tracking is possible. Depending on the camera and the optical train, uncertainties range from a few hundreds of micrometers to a few millimeters. For instance, photogrammetric techniques based on imaging of the whole ablator surface allow us to reach a higher resolution requiring a sophisticated setup and calibration procedure [19].

G. Main outcomes on the state-of-the-art review

Only the high-speed camera technique is found to be non-intrusive and versatile for any type of TPS materials. It is suitable for ground testing facilities but unfortunately, it cannot be used in-flight. The other measurement techniques have their own limitations, in particular their intrinsically intrusive nature and poor accuracy, typically equal or greater than 2 mm. The ultrasonic sensor-based method seems to be the most promising technique but not suitable for materials such as cork-based TPS.

III. Dual Field of View Measurement Technique

The measurement technique presented in this section requires only an optical access through the TPS. As shown in section VI, the RS instrument is flown on the reentry platform QARMAN in combination with an emission spectroscopy payload for which a similar optical access is needed. It allows us to have a combined RS/radiation measurement at the same location, which is optimal for collecting flight data. The sublimation process is measurable by the RS payload as a particular recession process that can be quantified for materials, such as Polytetrafluoroethylene

(PTFE), for which no pyrolysis is involved since its sublimation starts at 600 K. Existing measurement techniques cannot capture this sort of behavior, for example, the ARAD sensor uses resistive wounds (Nickel and Platinum) melting at temperature above 1700 K.

Our payload is based on the observation that the collection solid angle of a detector within a space platform changes during the mission when the canal through the TPS is cylindrical. For instance, this angle decreases when the TPS material swells (e.g. cork P50 at low enthalpy), while it increases when the material only sublimates (e.g. PTFE) or fully ablates (e.g. cork P50 at high enthalpy or ASTERM^{TM}). This observation led us to propose a method to measure the variation of thickness of a thermal protection material due to the RS phenomena with minimal modifications to the existing emission spectroscopy payload, as presented in section VI.

The basic idea of the proposed method is to track the change in emission intensity received by an Optical Measurement Device (OMD) as the viewing angle varies under the effect of RS. As shown in Fig. 7, recession produces a reduction of the canal length, whereas swelling increases the canal length. Thus, the field of view changes according to RS phenomena for the Optical Measurement Device with Modulated viewing angle (OMDM). However, the intensity of the emission coming from the plasma also changes in time during flight or during testing in ground facilities. To track the changes in plasma intensity, a second detector is used, the Optical Measurement Device of Reference (OMDR). This second detector has a fixed viewing angle that is smaller than the minimum expected viewing angle (e.g. maximal swelling). The idea is then to relate the changes in canal geometry by using the ratio of the OMDM signal to the OMDR signal. A reliable measurement of the change in canal geometry is thus obtained, even if the flight or testing conditions vary in time.

In practice, the OMDM detectors measure the total emission intensity $I_{tot}(t)$ for a given time taking into account the effect of canal length evolution. The emission intensity $I_{ref}(t)$ is measured by means of the OMDR detector, for which the solid angle is fixed. The ratio $\Delta\frac{I_{tot}}{I_{ref}}$ can be related to the change in solid angle through a canal of radius $\boldsymbol{c}$, hence to the change in canal length $\boldsymbol{l}$ through the following relation:

$$\Delta\frac{I_{tot}}{I_{ref}} \propto \Delta\Omega \propto \sin\Theta\,\Delta\Theta, \tag{1}$$

with $sin\,\Theta = c/(l^2 + c^2)^{0.5}$. To save space for integration in the platform, the I_{tot} and I_{ref} measurements are done at the same location by means of a beam splitter based on metallic coating (50%/50% ratio). The OMDR uses two

pinholes to constrain the field of view and proceed to the I_{ref} measurement (see following section). For the I_{tot} measurement, the OMDM is directly dependent of the length of the canal thus dependent of recession and swelling.

Fig. 7 illustrates the I_{tot} and I_{ref} measurements integration within the payload. In the figure, the light cone received by the OMDR stays constant whatever the amplitude of the RS. The light cone received by the OMDM. This surface increases in the case of recession as the length of the canal reduces. On the contrary, this surface decreases in the case of swelling because the length of the canal increases. Using the measured variations of the OMDM signal, normalized to the OMDR signal, the RS values can be obtained.

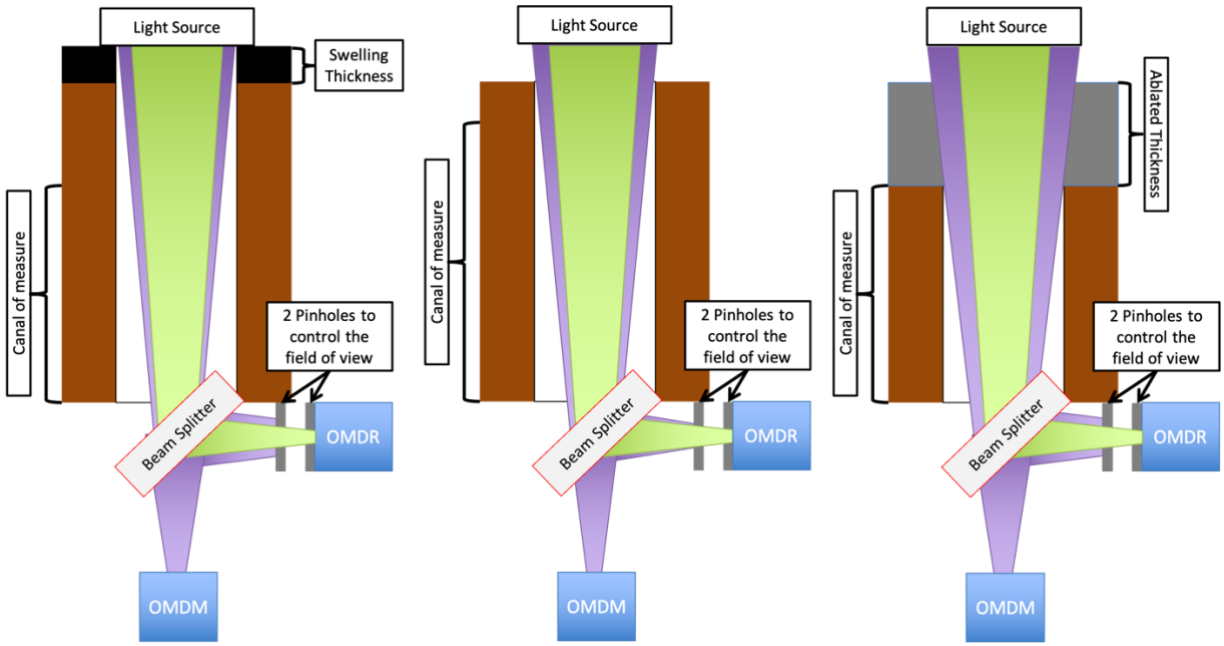

Fig. 7 Schematic measurement device (left: swelling case; middle: initial configuration; right: recession case).

IV. Constraining the Field of View

The main requirement of the proposed method for RS optical measurements is the ability to precisely constrain the field of view of one of the two OMDs, that is used as reference device (OMDR). For this, it is sufficient to position the two pinholes of the OMD with high precision. To this end, an alignment setup and a dedicated code were developed to choose the diameters and spacing of the pinholes in order to get the best accuracy for the measurement.

A. Light propagation code

Before aligning the pinholes, it is necessary to select the appropriate design constraints, namely the diameters of the two pinholes as well as their positions within the payload. To this end, a light propagation code was written. The code propagates the light from one boundary (plasma source) to another (OMDR), Fig. 8 illustrates the different parameters necessary to use the code.

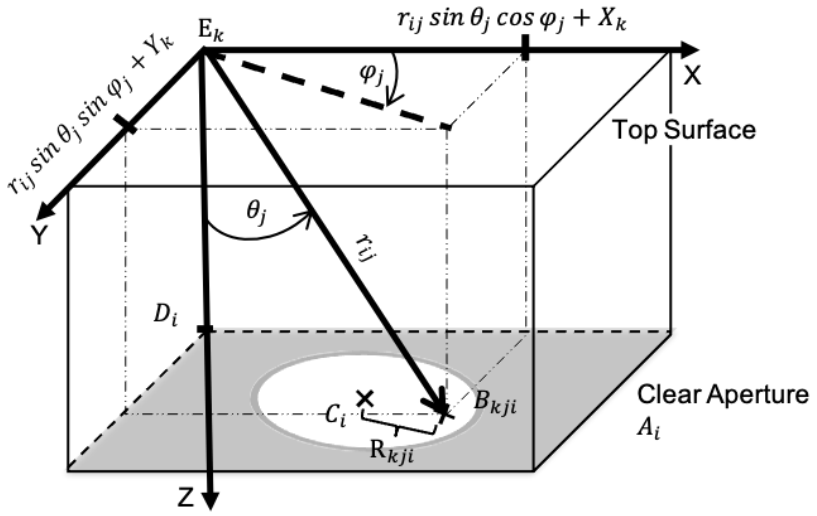

Fig. 8 Geometrical description of the parameters used for the light propagation code.

Elementary surfaces ds_k are defined at the first boundary (i.e. top surface of the TPS), where index k denotates the discretization of the disk. The centers of the ds_k elements located at the orifice of the measurement canal have three-dimensional coordinates denoted by $E_k = [X_k \quad Y_k \quad Z_k]^T$ with $Z_k = 0$. For each elementary surface ds_k, light rays are propagated at various angles θ_j and φ_j in a spherical coordinate system of center E_k where index j refers to the angular discretization. The values of θ_j and φ_j range from -90° to 90°, thus covering the hemispheric field of view turned towards the inside of the canal at uniform incremental angles $d\theta$ and $d\varphi$, respectively. The values of ds_k, $d\theta$ and $d\varphi$ depend on the desired precision and the relative size of the system. Through an iterative procedure going from the first interface to the last one (Top surface → 1st pinhole → 2nd pinhole → OMDR), the rays which do not reach the clear aperture of each interface are discarded (absorption on canal walls). We define the clear aperture A_i as the area of an interface, denoted by index i, of center coordinate $C_i = [X_{C_i} \quad Y_{C_i} \quad Z_{C_i}]^T$ and radius R_i, located at distance $Z_{C_i} = D_i$ from the light source. The intersection of the projected beam with the i^{th} interface plane, B_{kji}, is at a distance R_{kji} from the center of the aperture (C_i). The cartesian coordinates of the point B_{kji} are given by:

$$B_{\mathrm{kji}} = \begin{bmatrix} r_{ij}\, sin\, \theta_j\, cos\, \varphi_j + X_k \\ r_{ij}\, sin\, \theta_j\, sin\, \varphi_j + Y_k \\ D_i \end{bmatrix} \tag{3}$$

with

$$r_{ij} = {D_i}\Big/{\cos\theta_j} \tag{4}$$

R_{kji} is then given by:

$$\mathrm{R}_{kji} = \sqrt{\left(X_{C_i} - r_{ij}\sin\theta_j\cos\varphi_j - X_k\right)^2 + \left(Y_{C_i} - r_{ij}\sin\theta_j\sin\varphi_j - Y_k\right)^2} \tag{5}$$

For a ray to reach the clear aperture circle, R_{kji} must be less than the radius of the aperture, such that:

$$\mathrm{R}_{kji} \leq R_i \tag{6}$$

The propagated light domain determined in this manner can be visualized in Fig. 9. This figure corresponds to the following reference configuration (which actually corresponds to the optimum configuration presented in the following section). The reference configuration corresponds to a geometry with a canal length of 90 mm, canal diameter of 4 mm, and two pinholes of identical diameters of 0.3 mm, with a pinhole spacing of 14 mm and a pinhole standoff distance from the OMD of 2.39 mm.

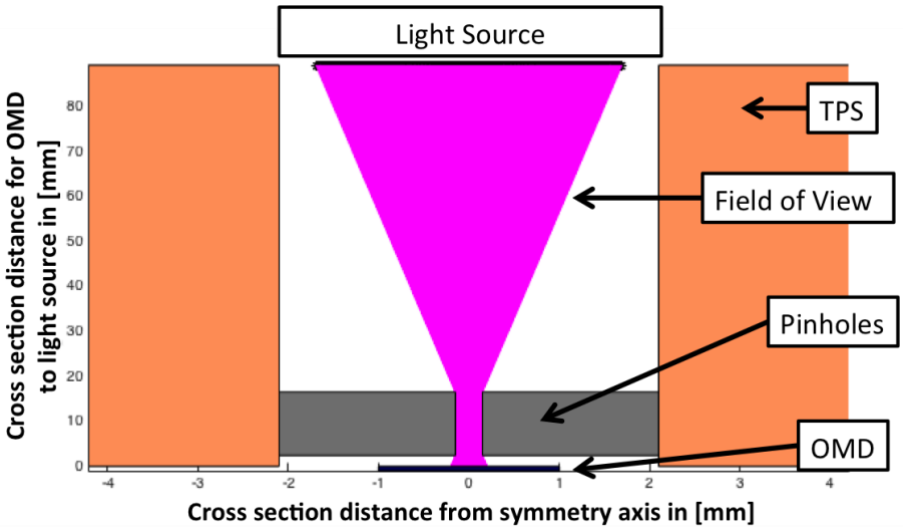

Fig. 9 Projection of light from the plasma source (top) to the OMD (bottom).

As shown in Fig. 9 the solid angle obtained is smaller than the maximal allowed one (i.e. the cone of light does not touch the walls of the canal). This precaution allows us to measure potential swelling of the TPS sample. Consider

two pinholes of radii r_1 are r_2, centered at the points $[X_1 \quad Y_1 \quad Z_1]^T$ and $[X_2 \quad Y_2 \quad Z_2]^T$, respectively. After some algebra, it can be show that the viewing solid angle is entirely determined by the pinhole geometry. Its intersection with the interface $Z = 0$ is a circle of radius equal to $|1-\lambda|r_1 + |\lambda|r_2$ that is centered at the point $[(1-\lambda)X_1 + \lambda X_2 \quad (1-\lambda)Y_1 + \lambda Y_2 \quad 0]^T$, with $\lambda = -Z_1/(Z_2 - Z_1)$. Changing the standoff distance between the pinholes and the OMDR only changes the light intensity transmitted onto the OMDR's active area. The standoff distance has to be selected to avoid saturation/damage of the OMDR's active area.

This distribution of light intensity projected onto the OMDR is calculated by integrating the contribution of each light ray ($\mathrm{d}\Phi_{OMD}$) transmitted to the OMDR using its position and relative angle with the OMDR plane ($90 - \theta$) according to the following relation:

$$\mathrm{d}\Phi_{OMD} = \mathrm{I}_k ds_k \cos\theta_j \sin\theta_j \, d\theta_j d\varphi_j \tag{7}$$

Where I_k is the intensity emitted by the elementary surface k expressed in W. m^{-2}.

Fig. 10 presents the projected power of the light source on the OMDR, calculated using Eq. 7. The code user will have to characterize the light source and choose a standoff distance to match the limits of the selected OMDR.

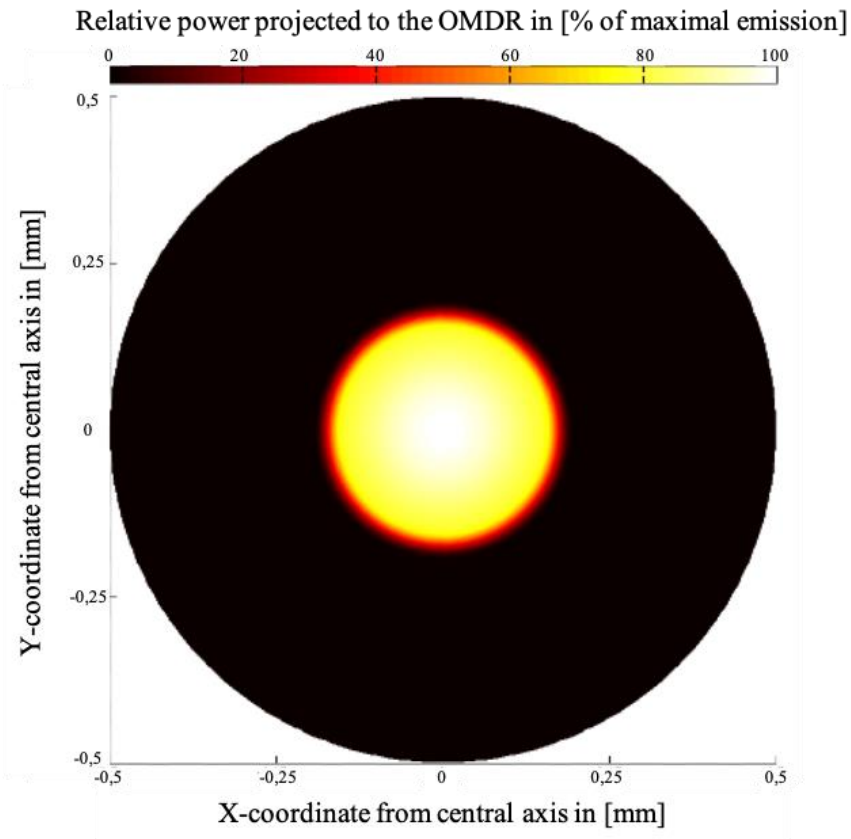

Fig. 10 Image of the projection of a uniform light source onto the OMD through the two pinholes in [%] of the original light source intensity (reference configuration of Fig. 9).

As expected, the pinholes cast a shadow on the OMDR by controlling the field of view. An OMDR with a small active area will then be preferred to maximize the signal-to-noise ratio.

B. Pinholes setup optimization procedure

The light propagation code developed allows us to assess the effectiveness of each triplet of parameters (pinhole 1 diameter, pinhole 2 diameter, pinhole spacing) linked to the angle-constrained design. By propagating the set of triplets, it is possible to identify the optimal design.

To limit the parameter space, we restrict ourselves to a range of commercially available pinholes (diameters: 1, 2, 5, 10, 15, 20, 25, 30, 40, 50, 75, 100, 150, 200, 300, 400, 500, 600, 700, 800, 900, 1000 µm) and to a pinhole spacing ranging from 2 to 20 mm with a step of 2 mm. The efficiency coefficient used to assess the result of the simulation is defined as the integrated power projected on the light source normalized by the maximal value, this allow to maximize the signal to noise ratio. The results are presented in Fig. 11.

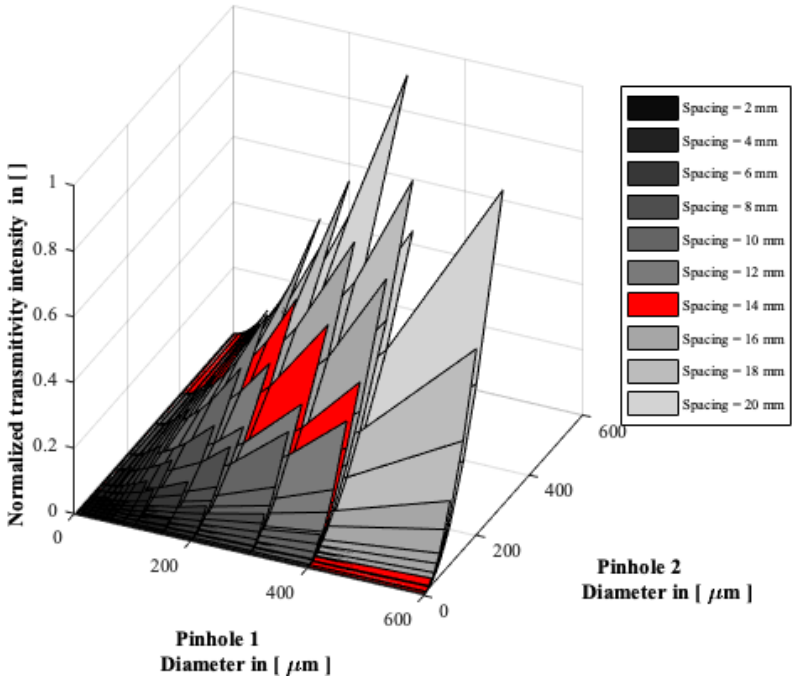

Fig. 11 Visualization of the light propagation simulation for the available configurations.

For each pinhole spacing available, the simulation gives a family of surfaces. The 14 mm pinhole spacing corresponding to the results presented in Fig. 9 and Fig. 10 has been selected as the maximum spacing possible according to the QARMAN mission constraints. To characterize the sensitivity of the alignment, Fig. 12 shows the solutions obtained for a spacing of 14 mm with a refined mesh of pinholes diameters.

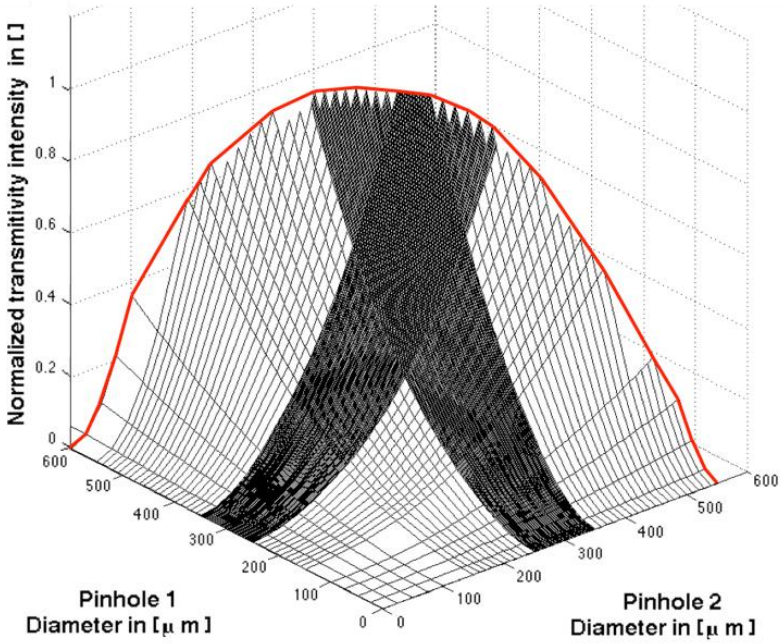

Fig. 12 Visualization of the light propagation simulation for pinhole spacing of 14 mm.

From the light propagation code, a maximum angle can be identified beyond which the emission collected by the OMDR is affected by the RS. This maximum angle corresponds to the light cone (OMDR field of view in Fig. 7) touching the walls of the canal (at maximum expecting swelling). The upper limit of the optimization plot (border to the surface line in Fig. 12) corresponds to pinhole dimensions beyond which the emission collected by the OMDR is affected by RS.

In this case, the alignment precision needed is simply the distance between the solution chosen (here two 300 μm diameter pinholes) and the limit of largest associated pinhole (intersection between the 300 μm diameter curve and the border to the surface in Fig. 12 yields a diameter of 375 μm). The alignment precision for the chosen pinholes and their spacing is then 75/2=37.5 μm from the central axis of alignment. It means that if one of the two pinholes is positioned farther than 37.5 μm from the central axis, the setup will not be able to provide a correct controlled field of view and the canal length will directly affect the field of view. Fig. 13 shows the maximal misalignment admissible (reference configuration) for the OMD measurement to not be affected by RS. The field of view with perfect pinholes alignment is compared in Fig. 9 to the field of view for the maximal misalignment of 37.5 μm of the lower pinhole. As expected, the misalignment causes the field of view to touch the wall of the canal.

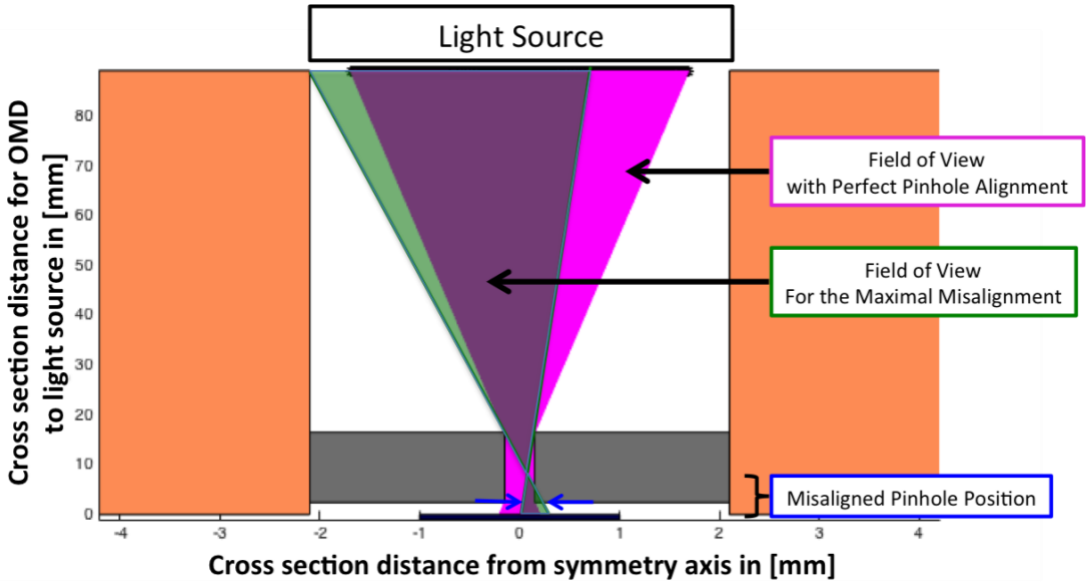

Fig. 13 Maximal misalignment admissible of one of the pinholes (bottom one here).

It has to be noted that larger pinhole spacing will allow for more comfort for alignment and a better measurement accuracy. But for the flight opportunity presented in this paper (section VI), we recall that the maximal allowable pinhole spacing is 14 mm in order to allow the integration of the instrument within the reentry platform.

C. Alignment of the pinholes

To ensure a correct measurement of recession, it is important to stay within the alignment precision defined in the previous part. The present case imposes an alignment accuracy below 37.5 µm. Such an alignment will also permit to measure swelling of the TPS material.

1. Alignment setup

Achieving a precise alignment with an accuracy on the order of a few tens of microns is a complex and non-trivial procedure. To this end, we use a digital microscope and micrometric displacement platforms as shown in Fig. 14.

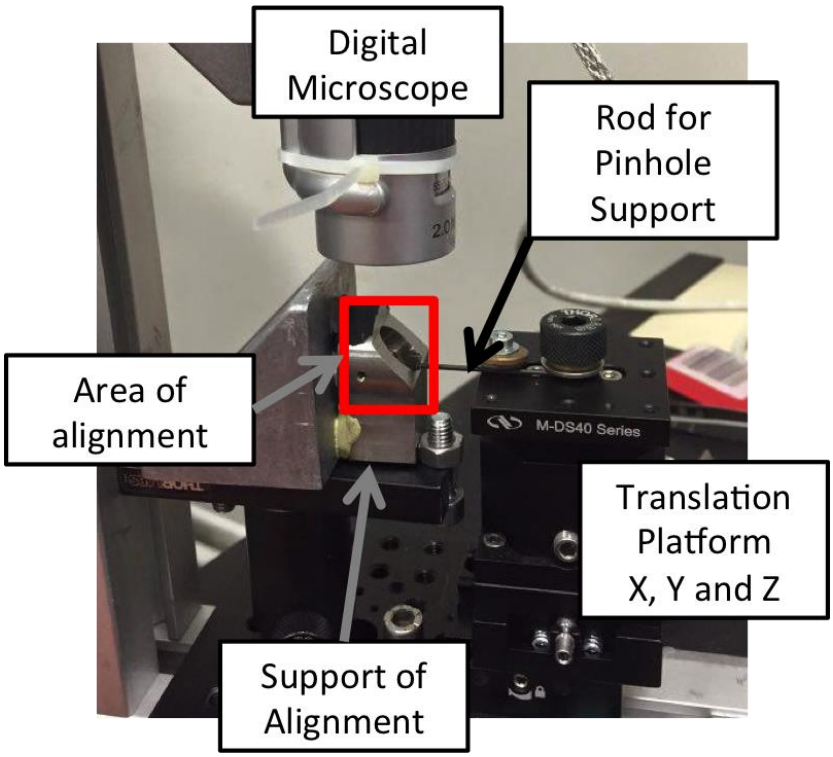

Fig. 14 Pinhole alignment setup.

An in-house software was written to automatically acquire images from the digital microscope and analyze the images with MatLab to detect the center of the pinhole. The center detection procedure is presented in the following section.

2. Center Detection

The best method to align objects (cylinders, holes…) is to detect and align their centers. An automatic procedure was implemented to detect the center of the different components of the system (2 pinholes and 2 alignment supports). For this purpose, the Adaptive Hough Transform (AHT) [20] has been implemented. Derived from digital image processing techniques, it relies on edge detection as input.

Edge detection is performed by calculating the double gradient of the black and white color map of the microscope picture in both X and Y directions producing a table containing coordinates of pixels (TE) where suitable gradients have been detected. Depending on the desired sensitivity, a certain number of contours (Fig. 15) are detected as edges.

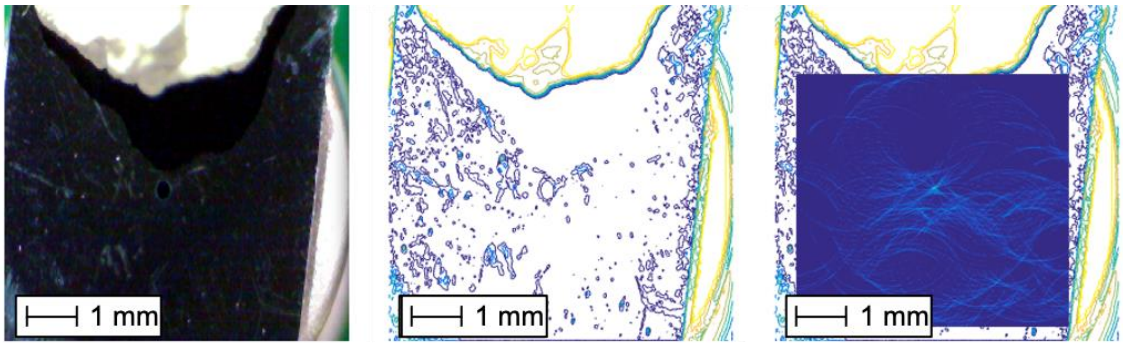

Fig. 15 Contour detection of a 300 µm pinhole located in the center of the image (left: pinhole under microscope; middle: detected contours, right: microscopic picture overlaid with intersecting circles showing the center at the center of the image).

Due to the imperfection of the physical process for picture acquisition and to imperfections on sample surface, the contours are always imperfect (blurry lines and edges too thin to be detected with the considered pixel resolution). For this reason, the AHT is used to group edges and propose circle candidates. Sensitivity parameters (range of possible diameters and background/foreground gradient ranges) permit to discriminate among these candidates to identify only one center.

The first step of the procedure is to divide the initial picture into a Fine Mesh Grid (FMG), as fine as the accuracy that can be achieved in the physical alignment system. Then, an iterative loop is introduced. The code starts with a specific diameter of pinhole to detect within the range specified (D_1 to D_N, specified by the user).

For a given iteration i with D=Di, the code goes to the location of each detected edge ($E_{current}$ a pixel for TE) and calculates the location of a circle of diameter D_i and center $E_{current}$. The position of the circle is then interpolated with the FMG. Each interpolation location is considered as a vote in the AHT process. When the loop is finished, the FMG then comprises either uniform data or sharp peaks. Uniform data are associated with the absence of circles of diameter D_i in the picture. In the latter case, the location of each peak is the center of circle(s) of diameter D_i with a weight W_i representative of the number of votes. The code will continue to iterate for each potential diameter (up to D_N). At the end of the run, the pixel of FMG with the highest weight W_i is selected as center of the pinhole.

As observed in Fig. 15, an application of the AHT method detects numerous edges, more than just the edges of the pinhole due to surface imperfections. An example of center detection for a pinhole of diameter 300 µm. The voting process permits to efficiently discriminate between false centers and the true pinhole center.

The algorithm is rather computationally time intensive. Increasing the grid size or reducing the number of possible candidates permits to reduce the computational time. The geometry does not change over time, thus once the pinhole diameter is clearly identified, the procedure seen before can be run for only one diameter after the first time step to speed up the simulation. It is also possible to do a two-step FGM to save some computational time. The idea is to do a first quick run of the code with a coarse mesh and a second one with a fine mesh restricted to a small patch close to the center detected in the first run.

3. Positioning of the Pinholes

While the Adaptive Hough Transform is able to detect centers, the main idea of the pinhole alignment procedure is to align a pinhole with an optical path (i.e.: alignment support, see Fig. 14). To this end, a dynamic AHT is used to detect the change of position of the pinhole over the alignment support. The 3-axis displacement platform permits to control the position of the pinhole at the micrometric scale. Once the pinhole is correctly centered over the alignment support, space rated glue is applied to secure its position and dynamic AHT continues to run to track any possible deviation during the polymerization. With this method and the hardware used here, no deviation of the pinhole alignment was observed for the flight hardware described in section VI.

D. Measurement accuracy

The accuracy of the proposed method depends on the choice of the OMDs. An upper boundary can be estimated for the case of 10-cm recession in a typical LEO reentry. In this case, and with basic OMDs (two photodiodes), a 0.02 mm precision can be achieved.

For this purpose, a basic 12-bit acquisition system for the photodiodes is used. Putting the upper limit (111111111111) on 10 cm of ablation and the lower limit (000000000000) on the initial condition, i.e. 0 cm of ablation, 4096 levels are available to code the recession giving 100 mm/4096 = 0.0024 mm accuracy.

This method is more accurate than most instruments used for missions and ground test facilities presented in the state-of-the art. Its performance is comparable to the ultrasonic-based technique but is suitable for any type of TPS, also allowing us to measure swelling.

V. Performance of the Measurement Technique

In this section, we assess the RS measurement technique for a cork-based TPS, for which both swelling and recession can occur. A sample of Cork P50 from Amorim™ was exposed to a plasma produced in the VKI Plasmatron [18]. The facility is equipped with a 160 mm diameter inductively coupled plasma torch powered by a 400 kHz

frequency, 1.2 MW power, and 2 kV voltage generator. The gas is heated by induction through a coil, creating a high-purity plasma flow. For the results presented here, atmospheric air at a mass flow of 16 g/s is used to produce a subsonic plasma flow. The stagnation point heat flux measured by means of a water-cooled calorimeter is equal to $2MW/m^2$. The static pressure in the chamber is 100 mbar. The sample is attached to a sample holder located 445 mm downstream of the plasma jet exit. After reaching the target testing condition (static pressure and heat flux), the sample is inserted into the plasma jet using a pneumatic mechanism.

In addition to the instrument embedded within the test sample, a high-speed camera was installed outside the facility to observe the swelling and recession. The short exposure times (2 μs) of the Vision Research Phantom 7.1 CMOS high-speed camera are used to prevent sensor saturation. The sample's surface radiates as a grey body and its edge can be tracked from pixel to pixel to determine swelling/recession as described in subsection II-F. The accuracy of RS tracking with the high-speed camera is limited by the size of the CCD pixels. Fig. 16 shows a comparison between the measurements obtained with our system and the high-speed camera. The plot shows the absolute value of recession distance, with 0 being the position of maximal thickness (virgin material).

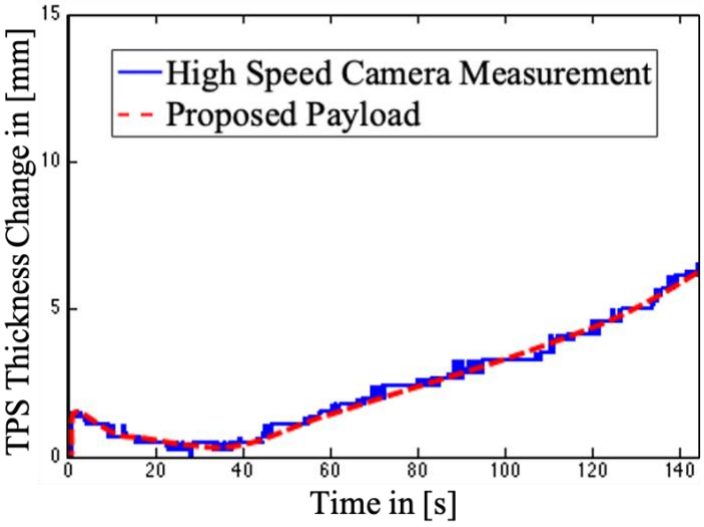

Fig. 16 Cork P50 material sample response during Plasmatron testing: swelling [1-30s] and recession [30-140s] (broken line: proposed instrument; unbroken line: high-speed camera located outside of the testing chamber).

For the full duration of the testing), the results shown in Fig. 16 demonstrates that there is excellent agreement between the two measurement methods. As expected, the high-speed camera measurement (blue) is not smooth and varies in steps (determined by the camera's pixel size). The payload measurement result (red) shows a smooth curve.

The latter method is able to accurately track both swelling and recession without saturation of the measurement and with high signal-to-noise ratio.

An additional test was performed with a sample without any measurement canal (not shown here). This test demonstrated that the optical access of the measurement technique presented in this paper does not influence the RS process, thus, the technique can be considered as non-intrusive for the thermal response of the TPS.

VI. QARMAN Mission

A. Flight Opportunity

The RS measurement technique presented in this paper is part of the INES (Imbedded Nano-size Emission Spectrometer) instrument which allows to measure reentry plasma radiation at the same location (through a common optical access) as the TPS thickness tracking. This instrument integrated within QARMAN (QubeSat for Atmospheric Research and Measurement on AblatioN) benefits from two technologies patented by ArianeGroup [[21], [22]]. This platform developed by the von Karman Institute is the world's first CubeSat designed to survive atmospheric reentry. The main aim of the QARMAN mission is to demonstrate the usability of a CubeSat platform as an atmospheric entry vehicle.

QARMAN is a parallelepipedal satellite of 34x10x10 cm^3 volume for a 5.2 kg mass respecting the 3U CubeSat standard, fitted with deployable solar panels (Fig. 17). Approximately 1/3 of the volume is devoted to the Thermal Protection System, made of Amorim™ cork P50. The TPS is instrumented by means of thermocouples and pressure plugs and hosts the INES payload described in this paper.

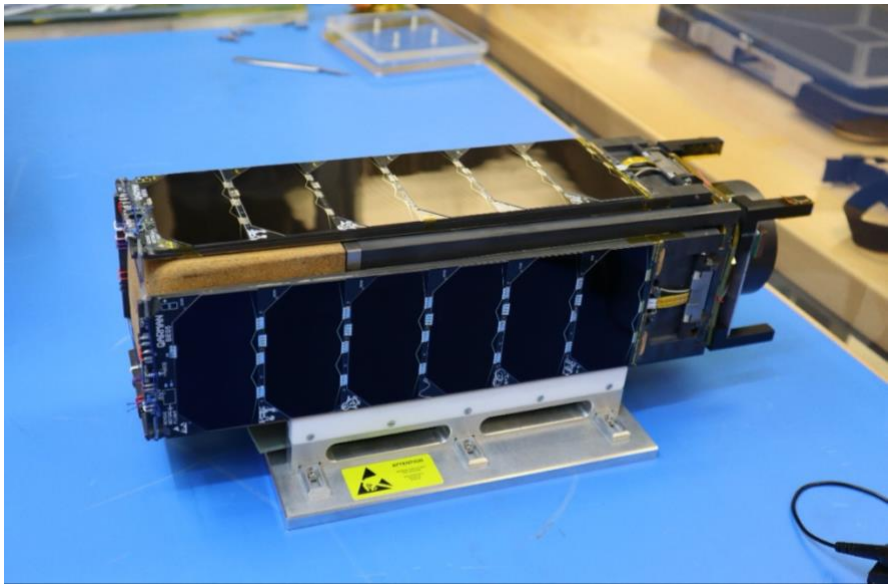

Fig. 17 QARMAN flight model in stowed configuration.

Fig. 18 presents the mission scenario of the QARMAN mission going from orbital deployment to atmospheric reentry. It can be divided into 4 sub-phases as seen in the figure and explained in the following sections.

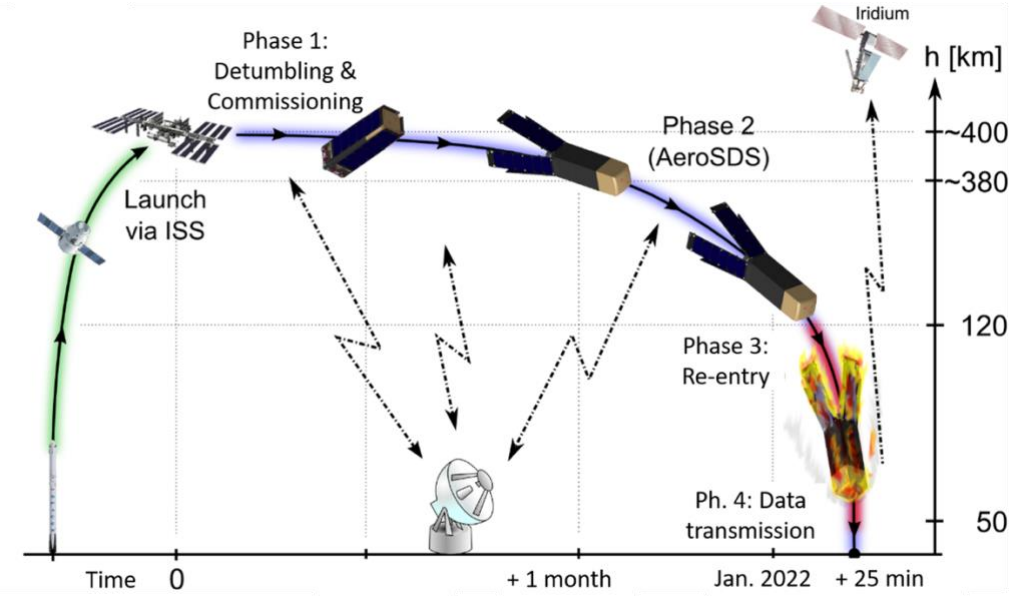

Fig. 18 The QARMAN mission consists of 4 phases with a deployment into orbit from the International Space Station on February 9th, 2020.

1. *Phase 1: Commissioning & Detumbling*

Right after deployment from the International Space Station, at an altitude of approximately 400 km, the commissioning phase starts. The vital subsystems are booted and the UHF antennae are deployed after 45 minutes in

order to establish the first ground contact. Using magnetorquers, the satellite is detumbled and stabilized from the initial tumbling rates (expected to be below 10 deg/sec). The performances of each subsystem are then assessed in order to reach full commissioning of the platform. This phase is expected to last from a minimum of 2 weeks up to one month in the nominal scenario.

2. *Phase 2: AeroSDS*

At the end of phase 1 after 1 month of operations in orbit, the AeroSDS panels, consisting of the ceramic panels with integrated solar cells, are deployed into a dart configuration with an angle of 15 degree with respect to the satellite longitudinal axis. The system provides aerodynamic stabilization and an increased drag area, progressively reducing the satellite altitude faster compared to the stowed configuration.

3. *Phase 3: reentry*

Phase 3 is the reentry, which can be considered the core part of the mission, where the major return for the science campaign and technology validation is expected. This is also the most critical part of the mission, as the satellite is subject to very high temperature and hypersonic velocities. While the satellite reenters through the upper atmosphere at a speed up to Mach 27, a thermal protection system is used to protect the electronics, based on high-technology insulation (Pyrogel and FiberFrax materials and ceramic walls) and ablative material (AMORIM^{TM} Cork P50).

4. *Phase 4: data transmission*

The plasma flow surrounding the satellite during the reentry phase causes a communications blackout, where no data can be transmitted to mission control. The acquired data of phase 3 is stored and compressed on flash memory and transmitted towards the Iridium constellation once the blackout has terminated. The beginning of phase 4 is expected at an altitude of 45 km. The data budgets are calculated such that all data can be safely transmitted in the short time frame between the end of the black-out window and the satellite's impact on Earth's surface.

QARMAN has been deployed into orbit from the International Space Station on February 9th, 2020. Currently, the platform is orbiting in space in deployed configuration (phase 2). It is expected to reenter Earth atmosphere in January 2022.

B. INES Instrument Setup

The INES instrument is located inside the heatshield of QARMAN. The following sections review the design of the smart plug (cavity and RS measurement part) and the spectrometer casing and the pinhole alignment for the instrument.

1. Smart plug and spectrometer casing

The INES payload is composed of an emission spectrometer (STS-VIS [23] as OMDM), a photodiode (FDS-010 [24] as OMDR), a 777 nm filter (FL05780-10 [25]), a beam splitter (BSW25 [26]) to split the light between the two OMDs, a sapphire window (WG31050 [27]) and an optical path able to protect the payload bay from extreme temperature without compromising the light transmittance and still measure RS. To illustrate the arrangement, Fig. 19 shows a cross section of the instrument. The cavity present in Fig. 19 allows for optical measurement without contamination of the optical path, as explained in a companion paper [28].

With a total mass of 350g and a volume of 260 cm^3, this design is light-weight non-bulky solution for reentry platforms in need for a flexible radiation and RS measurement payload. To satisfy launch and reentry loads, the structure of the payload is made of machined titanium. Fig. 20 illustrates the flight instrumentation hardware prior to the final integration into QARMAN.

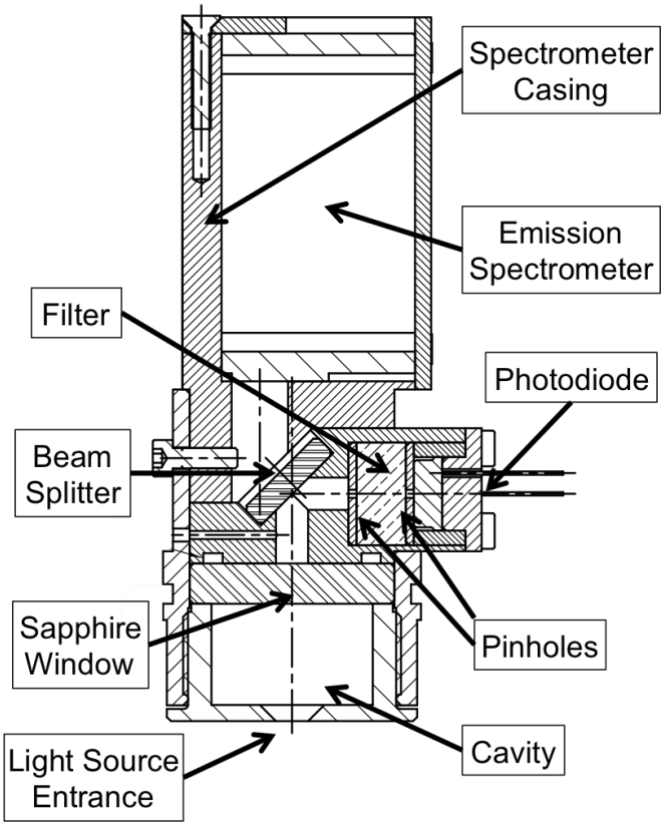

Fig. 19 Cross section of the INES payload with the different components

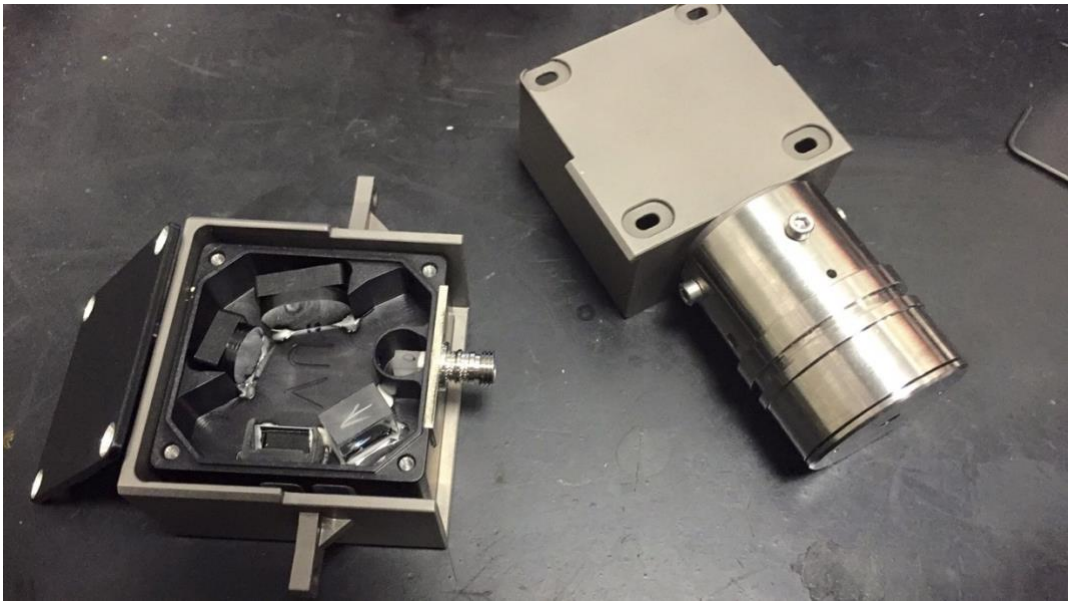

Fig. 20 Full payload prior to final assembly for pre-flight testing (left: emission spectrometer casing; right: smart plug casing).

2. Pinhole alignment procedure

The AHT code and alignment hardware (following the procedure of section IV-C) have been used to place two 300 μm pinholes for RS measurement on the payload and to fix them with EP30-3LO space rated glue [29]. Fig. 21 shows details of the pinhole alignment process. The figure shows, from left to right, the calculation of the solid angle, the support of alignment, the pinhole positioned and the precision of alignment.

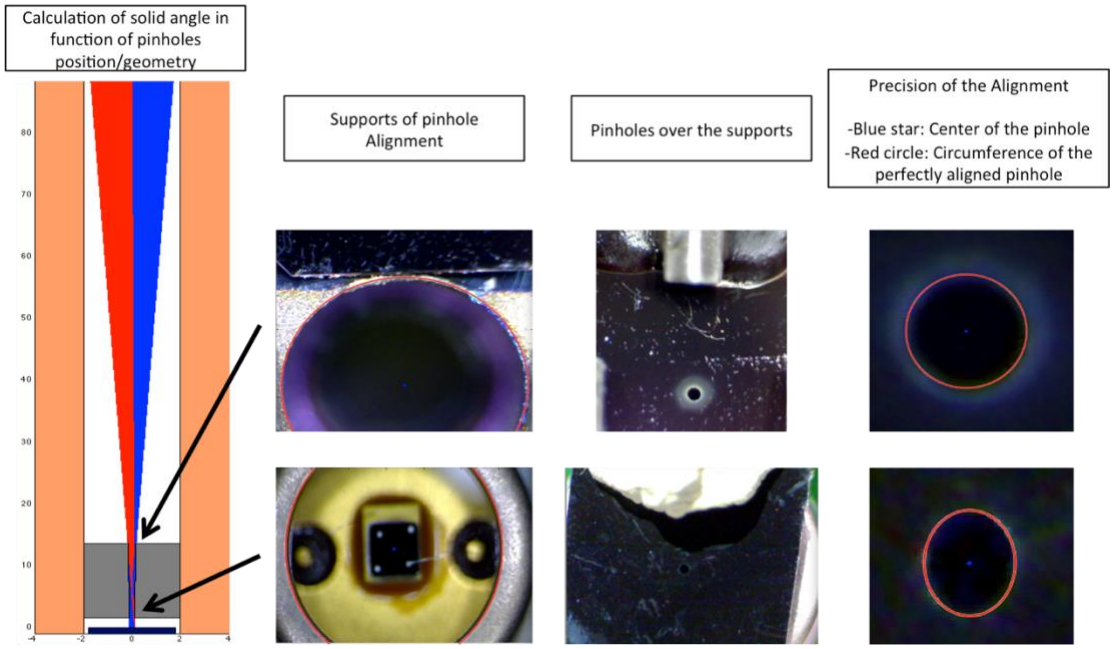

Fig. 21 Full Pinhole alignment process for 2 pinholes (300 µm diameter) for the RS part of the instrument on INES.

The alignment method enabled us to center the pinholes within 5 µm of the perfect position. With this positioning accuracy, the RS instrument is able to measure recession range of the TPS thickness and the swelling of the TPS can be measured up to 7 mm (larger than the expected maximal swelling).

3. Alignment during mission

To ensure structural robustness of the mechanical design, special attention has been devoted to the material selection, casing design, numerical simulations and post vibration testing checks. We recall that the casing of the payload is made out of titanium. The material thickness has been selected to withstand both launch and reentry loads without deflection of the center axis larger than 15 µm at the beam splitter location (representing about half the maximal allowable deflection).

No deflection has been observed in simulation results for the reentry due to launch load dimensioning. For the launch loads, the payload has been tested for vibration within the QARMAN spacecraft; data acquired by the payload have shown no alteration of alignment nor performances. It is thus expected that the optical alignment will remain acceptable during the reentry phase when the measurements are performed. For a more constraining environment such as a mission requiring pyrotechnic separation, further evaluation of the pinhole alignment will be needed.

C. Mini-INES Configuration

Planetary exploration vehicles tend to be highly constrained in terms of the mass and volume available for scientific instruments. In order to propose a solution for the most constrained platforms, we studied and proposed a downsized version of the INES payload. This miniature configuration does not measure spectra, but rather the total radiative flux. It also measures RS, using two identical photodiodes and a beam splitter. The RS measurements have the same resolution as with the standard INES payload (0.02 mm for 14-bit coding). Fig. 22 shows a 3D drawing of the Mini-INES configuration.

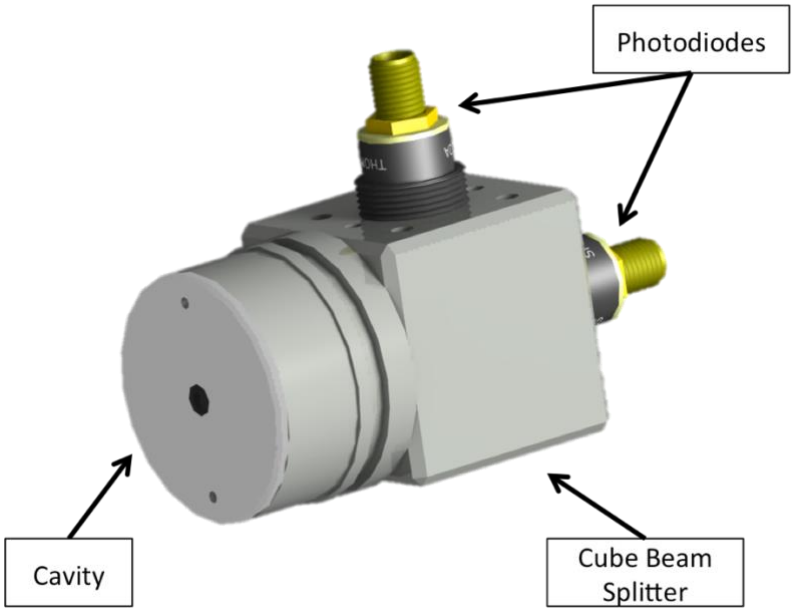

Fig. 22 Mini INES for simultaneous RS and total radiation measurements.

VII. Conclusion

The paper reviews the main solutions developed for instruments to measure recession (including sublimation) and swelling of TPS materials for heatshields. The limitations of existing RS instruments are discussed in terms of bulkiness, accuracy, TPS suitability, and intrusiveness. From this analysis, the ultrasound-based instrument is a promising technique but not suitable for our application, as it is not able to produce result for a certain range of TPS materials (including cork-based materials) without intrusive modifications of the TPS. We have developed a measurement technique that consists in using two radiation measurement devices (an emission spectrometer and an additional photodiode in the case of INES for QARMAN), each sensing a different solid angle. The emission

spectrometer observes a change in solid angle due to the variable length of the optical access (TPS thickness), while the photodiode keeps a constant solid angle thanks to two carefully positioned diaphragms. The ratio of both measured light intensities (at the same wavelength) is only dependent of the canal length, thus allowing us to quantify RS during flight.

Although conceptually simple, the instrument proposed requires optimization of the design parameters in order to be able to measure the full range of RS. For that purpose, a software was specifically developed to optimize the accuracy of the instrument. Based on the adaptative Hough transform, it allows for micrometric positioning (centering) of the two pinholes to reach RS measurement accuracies with an uncertainty lower than ±0.02 mm.

To illustrate the methodology on an ongoing demonstration mission, the INES instrument for the QARMAN mission was introduced. It allows us to perform coupled radiation/recession measurements without the limitations of the existing instruments reviewed. The full flight payload weighs 350 g, including a 68 g emission spectrometer (336-822 nm spectral range with a resolution of 1 nm) and a 5 g photodiode (777 nm). The Mini-INES version only measures the total radiative flux and the RS. Performing coupled measurements of radiation and RS at the same location is a clear advantage compared to existing solutions. This coupled measurement of the INES and Mini-INES instruments represents a light-weight non-bulky solution for instrumentation of future entry/reentry missions, especially for their capabilities to be used with any TPS material.

Acknowledgments

GB has received funding for this work from the ANRT with the ArianeGroup CIFRE grant #0064/2013. The QARMAN project was supported by an ESA GSTP grant #4000109824/13/NL/MH.

References

[1] E. Venkatapathy, C. E. Szalai, B. Laub, H. H. Hwang, J. L. Conley and J. Arnold, "Thermal Protection System Technologies for Enabling Future Sample Return Missions," in *White Paper to the NRC Decadal Primitive Bodies Panel*, 2009.

[2] O. Chazot and F. Panerai, "High-Enthalpy Facilities and Plasma Wind Tunnels for Aerothermodynamics Ground Testing," in *Hypersonic Nonequilibrium Flows: Fundamentals and Recent Advances*, pp. 471-521.

[3] D. Bose, M. Mahzari, J. Santos, K. Edquist, C. Kuhl, A. Little and M. Munk, "Performance of the MEDLI Integrated Sensor Plug (MISP) Hardware and TPS Response Reconstruction," in *10th International Planetary Probe Workshop*, San Jose, California, 2013.

[4] Thermometrics Corporation, "Thermocouples-Thermocouple Types- J, K, E, T, N, B, R, S," 2013. [Online]. Available: http://www.thermometricscorp.com/thermocouple.html. [Accessed 10 10 2018].

[5] I. Sakraker, E. Umit, T. Scholz, G. Bailet, P. Testani and V. van der Haegen, "QARMAN: An Atmospheric Entry Experiment on CubeSat Platform," in *8th European Symposium on Aerothermodynamics for space vehicles*, Lisbon, Portugal, 2015.

[6] M. M. Munk, "Application of the MEDLI Suite to Future Mars Entry Vehicles," in *Concepts and Approaches for Mars Exploration*, Houston, USA, 2012.

[7] J. M. Cassanto, C. R. DROMS and J. METZGER, "a Simple Recession Gage for In-Flight Measurement of the Char Degradation Zone for Re-entry Vehicle Heatshields," in *26th International Instrumentation Symposium*, Seattle, WA, 1980.

[8] J. C. Thomas, E. L. Petersen, B. B. Brady and J. Desain, "Hybrid Rocket Burning Rate Enhancement by Nano-Scale Additives in HTPB Fuel Grains," in *50th AIAA/ASME/SAE/ASEE Joint Propulsion Conference, AIAA Propulsion and Energy Forum*, Cleveland, USA, 2014.

[9] G. F. Gornostaev, V. V. Pasichnyi and G. V. Tkachenko, "Measurement of the ablation of heat shield materials by fiber-optical sensors," *Journal of Engineering Physics and Thermophysics 81(4):774-780*, 2008.

[10] J. A. Lloyd, M. Stackpoole, E. Venkatapathy and D. E. Yuhas, "A New, Non-Intrusive Ultrasonic TPS Recession Measurement Needed to Determine the Thermal Structure of the Upper Atmosphere of Venus, Saturn, Uranus or Neptune," in *International Workshop on Instrumentation for Planetary Missions*, Greenbelt, Maryland, 2012.

[11] G. Bailet, "Radiation and ablation studies for in-flight validation," CentraleSupélec, University Paris-Saclay, 2019. (to be published).

[12] H. Hwang, D. Bose, H. Wright, T. R. White, M. Schoenenberger, J. Santos, C. D. Karlgaard, C. Kuhl, T. Oishi and D. Trombetta, "Mars 2020 Entry, Descent, and Landing Instrumentation (MEDLI2)," *46th AIAA Thermophysics Conference.* https://doi.org/10.2514/6.2016-3536, 2016.

[13] R. A. Granger, Experiments in Heat Transfer and Thermodynamics, Cambridge University Press, 1994.

[14] A. Zibitsker, M. Berreby, R. Shilav and D. Michaels, "An ultrasonic method for ablation rate measurement of silica-phenolic TPS material," in *11th Ablation Workshop*, Minneapolis, 2019.

[15] M. Lingbloom, "Comparisons of NDT Methods to Inspect Cork and Cork filled Epoxy Bands," in *ASNT Fall Meeting*, Las Vegas, NV, 2007.

[16] Y. L. Hor, J. F. Federici and R. L. Wample, "Nondestructive evaluation of cork enclosures using terahertz/millimeter wave spectroscopy and imaging," *Applied Optics*, no. 47 (1), pp. 72-8, 2008.

[17] B. Helber, O. Chazot, T. Magin and A. Hubin, "Emission spectroscopic boundary layer investigation during ablative material testing in plasmatron," *Journal of Visualized Experiments*, pp. AIAA 2012-2876, 112: e53742, 2016.

[18] B. Helber, O. Chazot, A. Hubin and T. Magin, "Microstructure and gas-surface interaction studies of a low-density carbon-bonded carbon fiber composite in atmospheric entry plasmas," *Composites Part A: Applied Science and Manufacturing*, vol. 72, pp. 96-107, 2015.

[19] S. Loehle , T. Staebler, T. Reimer and A. Cefalu, "Photogrammetric Surface Analysis of Ablation Processes in High Enthalpy Air Plasma Flow," in *11th AIAA/ASME Joint Thermophysics and Heat Transfer Conference AIAA*, Atlanta, US, 2014.

[20] J. Illingworth and J. Kittler, "The Adaptive Hough Transform," *IEEE Trans. on Pattern Ananlysis and Machine intelligence*, pp. vol. 9, no. 5, pp. 690-98, 1987.

[21] G. Bailet, "Apparatus reduction liability of pollution of an optical access of an optical instrument". World Patent WO2018100255A1, 07 06 2018.

[22] G. Bailet, "Method and device for detecting and assessing a thickness variation of a workpiece". World Patent WO2018100256A1, 07 06 2018.

[23] Ocean Optics, 2018. [Online]. Available: https://oceanoptics.com/product/sts-uv-microspectrometer/. [Accessed 2018].

[24] Thorlabs, "FDS010 - Si Photodiode, 1 ns Rise Time, 200 - 1100 nm, Ø1 mm Active Area," 2018. [Online]. Available: https://www.thorlabs.com/thorproduct.cfm?partnumber=FDS010. [Accessed 10 10 2018].

[25] Thorlabs, "FL05780-10," [Online]. Available: https://www.thorlabs.com/thorproduct.cfm?partnumber=FL05780-10.

[26] Thorlabs, "BSW25 - Ø1/2" 50:50 UVFS Plate Beamsplitter, Coating: 350 - 1100 nm, t = 3.0 mm," 2018. [Online]. Available: https://www.thorlabs.com/thorproduct.cfm?partnumber=BSW25. [Accessed 10 10 2018].

[27] Thorlabs, "WG31050 - Ø1" Sapphire Broadband Precision Window, Uncoated," 2018. [Online]. Available: https://www.thorlabs.com/thorproduct.cfm?partnumber=WG31050. [Accessed 10 10 2018].

[28] G. Bailet, A. Denis, A. Bourgoing, T. E. Magin and C. O. Laux, “Passive method to measure reentry radiation in the presence of ablative products,” *Journal of Spacecraft and Rockets,* 2021. (to be published).

[29] MASTERBOND, "EP30-3LO Product Information," 2018b. [Online]. Available: https://www.masterbond.com/tds/ep30-3lo. [Accessed 10 10 2018].